THE JOURNAL OF PHYSICAL CHEMISTRY C
A JOURNAL OF THE AMERICAN CHEMICAL SOCIETY

pubs.acs.org/JPCC

Article

Polymorphism in $Na_2(Co/Zn)P_2O_7$ and $Na_2(Co/Fe)P_2O_7$ Pyrophosphates: A Combined Diffraction and ^{31}P NMR Study

Chiara Ferrara, Clemens Ritter, Piercarlo Mustarelli, and Cristina Tealdi*

Cite This: *J. Phys. Chem. C* 2022, 126, 701−708

Read Online

ACCESS | Metrics & More | Article Recommendations | Supporting Information

ABSTRACT: Pyrophosphates of the general formula $A_2BP_2O_7$ (A = alkali metal and B = transition metal) find applications in several technological fields, including rechargeable Na-ion batteries. They present a rich polymorphism vs composition, which may strongly influence their functional properties. Therefore, to selectively obtain a specific structure is crucial for applications. Here, we combine structural investigation techniques (solid-state NMR, X-ray and neutron diffraction, and DFT calculations) to investigate the crystal chemistry of the series $Na_2(M/M')P_2O_7$ with couples M/M' = Co/Zn and Co/Fe. For both the series, a phase transition vs composition is observed. A tetragonal to orthorhombic phase transition is found for the Zn/Co series, and an orthorhombic to triclinic phase transition is found for the Co/Fe series. Such changes are interpreted in view of the different electronic structures of the transition metal ion. In addition, with the support of modeling, short- and long-range structural analysis, we show that the coexistence of two polymorphs for a given composition is possible, suggesting that the final structures may be strongly dependent upon the synthesis procedure.

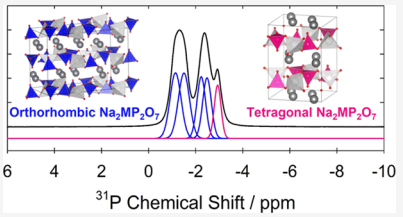

1. INTRODUCTION

Pyrophosphate compounds having the formula $A^I_2B^{II}P_2O_7$, with A = Na and Li and B = Co, Fe, Mn, Cu, and Ni, give origin to a wide variety of 2D and 3D crystalline structures in which the P_2O_7 units and BO_n polyhedra create a network where A ions may be accommodated.[1−5] Thanks to the combination of a robust inorganic open framework and the presence of the mobile A species, these materials are attracting attention for several technological applications (e.g., sensors, fuel cells, luminescent phosphors, catalysis, etc.).[6−8] In particular, $A^I_2B^{II}P_2O_7$ polyanionic oxides have been considered for the use in different compartments of sodium-ion batteries (SIBs). In fact, in addition to ionic conductivity, they can also offer high specific capacity, thanks to the presence of two Na ions per formula unit and good tailoring of the electrochemical properties, as different transition metal ions can be successfully introduced on the B site.[3,4,9−12] At the same time, it was observed that the substitution with different transition metal species leads to structural changes. Several polymorphs were found for different compositions, and more phases can be stabilized for a given composition by playing on the synthesis route and thermal treatments.[9,12−14] Since different structures can lead to different electrochemical responses, one of the main strategies to further improve the performance of the pyrophosphate family in the last years has been the introduction of mixed compositions of the general formula $Na_2M_{1-x}M'_xP_2O_7$, which can combine the electrochemical properties related to particular M/M' couples and the stabilization of different polymorphs. Some recent works presented the structural and electrochemical investigation of the solid solution $Na_2(Fe/Mn)P_2O_7$ series.[15,16] Several compositions related to the general formula $Na_2MP_2O_7$ with a wide range of M ions were already described and different structures reported in the literature, including tetragonal, orthorhombic, and triclinic crystal systems.[3−5,9,14,17]

Highly symmetric structures were found for the Zn and Co compositions. For the description of $Na_2ZnP_2O_7$, both small cell tetragonal $P4_2/mnm$[9,17−19] and large cell tetragonal $P4_2/n$[17] space groups were reported. In both these systems, the structure consists of ZnO_4 tetrahedra connected to P_2O_7 units forming five-member rings in continuous layers along the *ab*-plane. Na ions are placed below and above these planes, at the center of the rings. The overall structure is thus formed by $[Zn(P_2O_7)]$ layers alternated by Na ions (see Figure 1a−d). The connectivity is similar in both the space groups, the main difference being the eclipsed and partially eclipsed staking of the layers along the *c*-axis (see Figure 1b−d). Both the structures were reported for the Zn-based composition obtained under similar synthesis conditions.[17−19] A similar structural description is obtained also with the use of the orthorhombic space group $P2_1cn$,[4,14] where the partially eclipsed staking is maintained and a modulation of the layers along the *a* and *b* directions is visible (Figure 1e,f). Both tetragonal and orthorhombic cells were reported for the Co-based compound together with the triclinic phase. The layered forms were identified as "blue", whereas the 3D triclinic phase

Received: October 6, 2021
Revised: December 13, 2021
Published: December 22, 2021

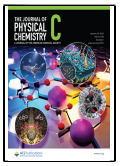

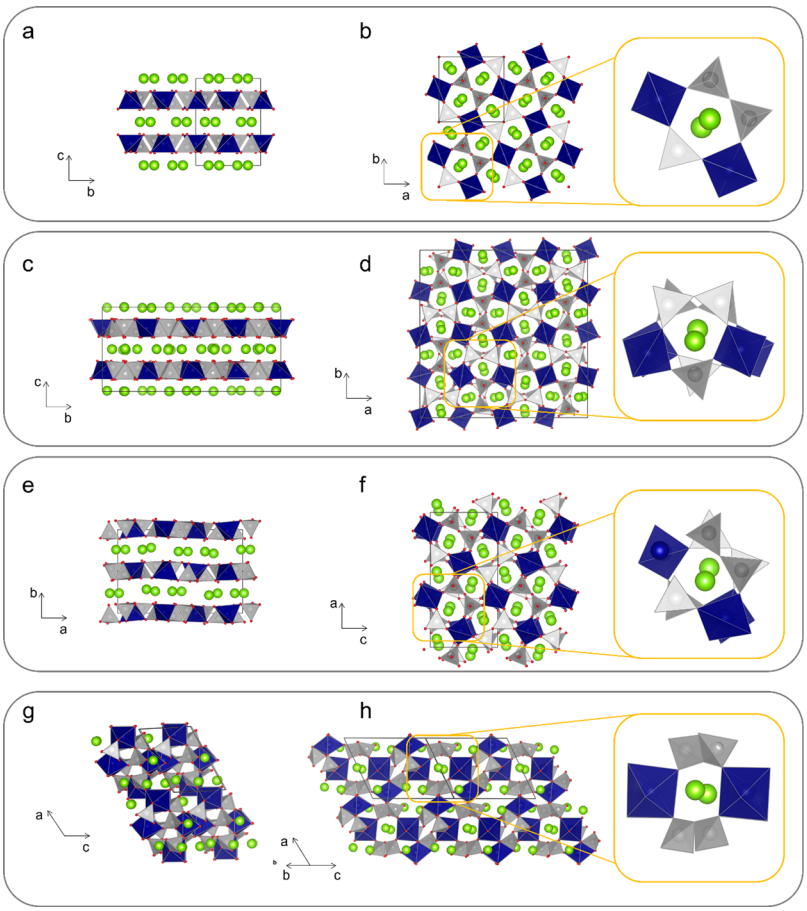

Figure 1. Structural models proposed for the $Na_2MP_2O_7$ systems. $P4_2/mnm$ small tetragonal cell view along *a* (panel a) and *c* (panel b) axes; $P4_2/n$ tetragonal large cell view along *a* (panel c) and *c* (panel d) axes; orthorhombic $P2_1cn$ cell view along *c* (panel e) and *b* (panel f) axes; and triclinic cell view along [001] (panel g) and [011] (panel h) directions. Na ions are represented in green, M polyhedra in blue, P tetrahedra in gray, O ions in red, and cell edges are marked with black lines.

was labeled as "rose" due to the intense colors of the final powders related to the different coordination and crystal field of the Co ions. The triclinic phase is the less stable, and the high temperature phases can be obtained upon heating of the triclinic form with phase transition taking place around 380 °C.[13] Whereas the high symmetry phases are very similar in terms of connectivity and ion coordination, the triclinic form is substantially different. The structure presents a 3D open framework described with *P*1[13,20] or *P*-1 symmetry.[10,14,21] The structure is made of corner-sharing dimers $[Co_2O_{11}]$, where the Co cations are in octahedral coordination. The dimers are interconnected with pyrophosphate groups $[P_2O_7]$. This 3D open network presents 1D channels along different directions ([100], [−100], and [01−1]), where the Na ions are allocated and where they can diffuse, as reported in Figure 1g,h. This phase was observed for the systems containing Co, Fe, and Mn.[10,13,15,21] All the described structures present 1D, 2D, or 3D pathways for the diffusion of Na ions, so making the whole class of compounds highly favorable for application in batteries.

In this work, the $Na_2(Co/Zn)P_2O_7$ and $Na_2(Co/Fe)P_2O_7$ systems will be discussed. The combined use of solid-state nuclear magnetic resonance (NMR), density functional theory (DFT), and diffraction techniques allowed a careful understanding of the phases obtained for the Co, Fe, and Zn compositions, chiefly by correlating the transition metal center with the final symmetry of the synthesized compounds.

2. MATERIALS AND METHODS

The powder samples of the series of mixed-metal compounds $Na_2MP_2O_7$ were prepared by the traditional solid-state route[3,15−17] starting from stoichiometric amounts of Fe(C_2O_4)*$2H_2O$ (Aldrich, 99%), Co(C_2O_4)*$2H_2O$ (Aldrich, 99%), ZnO (Aldrich, >99%), NaH_2PO_4 (Aldrich, 98%). The reagents were accurately mixed in acetone and the obtained mixture was then heated at 300 °C for 2 h to eliminate the organic components. The powders were ground again and pelletized, and underwent repeated treatments at 600−720 °C for 6 h with heating and cooling rates of 10 °C/min and with intermediate grindings until completion of the synthesis. The thermal treatments were performed under steady Ar flow for the Co- and Fe-containing samples to prevent oxidation of the transition metal ions. In case of the Zn-based sample, the synthesis was performed in air.

Samples were named according to the composition, with respect to the formula $Na_2Co_{1-x}(Zn, Fe)_xP_2O_7$, with the labels Co1 ($x$ = 0), Co75Zn25 (x = 0.25), Co50Zn50 (x = 0.50), Co25Zn75 (x = 0.75), Zn1 (x = 1), Co75Fe25 (x = 0.25), Co50Fe50 (x = 0.50), Co25Fe75 (x = 0.75), and Fe1 (x = 1).

Powder X-ray diffraction patterns were collected at ambient temperature and pressure on a Bruker D8 Advance powder diffractometer operating in a Bragg−Brentano geometry using the Cu-Kα wavelength. Scans have been collected in the

https://doi.org/10.1021/acs.jpcc.1c08753
J. Phys. Chem. C 2022, 126, 701−708

angular range 5−100° with a step size of 0.02 and acquisition time 10 s per step.

High-resolution, high intensity neutron diffraction data were collected at room temperature at the D2B beamline at the Institut Laue-Langevin, ILL in Grenoble (France). The samples were measured in a vanadium sample holder (no background subtraction needed). Data were collected in the angular range 0−160° with step size 0.05 using a wavelength of 1.594 Å.

Diffraction data were analyzed according to the profile matching Le Bail fitting[22] and with the Rietveld method[23] using the FullProf software[24] to derive cell parameters and unit cell volumes. The intensities of the reflections for all the XRPD patterns are affected by the severe preferred orientation effect. This aspect can significantly influence the results of accurate refinements; for this reason, only profile matching analysis was performed for most of the samples, as the main scope of our investigation was to follow the structural evolution and the variation of the cell parameters as a function of the composition. Rietveld refinement was performed only for two end members (Co1 and Zn1 samples).

Solid-state ^{31}P NMR spectra were collected on a Bruker Avance III 400 MHz spectrometer (9.4 T). The spectra were acquired using a 4 mm magic angle spinning (MAS) probe (spinning speed 10 kHz) using a one-pulse sequence with 90° pulse of 4.2 μs, a recycle delay of 100 s, and 64 scans. The pulse length and recycle delay were previously calibrated. The chemical shift was referred to an 85% solution of H_3PO_4 (0 ppm). Spectrum quantitative analysis has been performed with the use of the software Sola (embodied in the TopSpin 3.1 package) and DMFit.[25]

The DFT study was performed with the PWscf code embodied in the Quantum ESPRESSO package.[26] The Kohn−Sham orbitals were expanded in a plane wave basis set to a kinetic energy cut off of 600 Ry. The exchange correlation term proposed by Perdew−Burke−Ernzerhof (PBE) was used.[27] The total energy calculations have been carried out for the different polymorphs allowing for cell parameter and atomic position relaxation until the obtained forces were less than 0.001 eV Å^{-1} and the total energy differences less than 0.001 eV using a 6 × 6 × 4 and 2 × 6 × 4 k grid (Monkhorst-Pack scheme) for the small cell and the orthorhombic cell, respectively.

3. RESULTS AND DISCUSSION

For the following investigations, all the structural models previously described in the introduction (Figure 1) were considered. Data and results for the two series are reported separately in the following paragraphs.

3.1. Co/Zn Series. The $Na_2(Co/Zn)P_2O_7$ series was first considered. For the two end members, both the tetragonal and the orthorhombic polymorphs were reported, as a clear and unequivocal description of the symmetry of pure Zn and pure Co compositions is still lacking. Although for the Co composition also the low symmetry triclinic polymorph was observed, it will not be considered here, as it can be obtained only under particular synthesis conditions, not used in this study.

The $Na_2ZnP_2O_7$ end member was originally described using the tetragonal $P4_2/mnm$ space group, as shown in Figure 1a,b.[18] A subsequent single crystal diffraction study, with a detailed investigation of the allowed symmetry classes and possible reflections, led to the identification of a larger tetragonal cell as the preferred structural model (the so-called large cell tetragonal).[17] More recently, both these models were used for the description of $Na_2ZnP_2O_7$ with no further investigations on the structure.[19,28]

An equally uncertain situation is observed for the description of the $Na_2CoP_2O_7$ end member. In this case, only the small cell tetragonal and the orthorhombic models were proposed. Sanz et al.[9] already highlighted the similarities between these two structures, concluding that there were no significant differences between the two models and that the only existing layered structure was the tetragonal one. At the same time, a detailed study of Beaury et al. on the optical and magnetic properties of the $Na_2CoP_2O_7$ composition revealed the presence of several different local environments for the Co ions, compatible with the coexistence of the tetragonal and orthorhombic phases.[14] However, the magnetic moments obtained by Sanz and Beaury are very similar. Finally, while Sanz suggested that the tetragonal symmetry was enough for a satisfactory description of the system, more recently Barpanda et al. identified the orthorhombic phase as the unique product obtained under several different synthesis conditions.[29]

The XRPD patterns originated from structures with strictly related symmetry can lead to ambiguous identification of the phase(s). In fact, the small cell, the large cell tetragonal, and the orthorhombic structures present the same connectivity between the polyhedral and are all very similar. At the same time, a close inspection of the local environment and the symmetry for the different ions reveals significant differences. For example, just one crystallographic site is available for phosphorus in the small cell tetragonal model, whereas eight and four distinct positions are available in the large cell tetragonal and orthorhombic phases, respectively. Therefore, ^{31}P MAS NMR, which is sensitive to the local environment, can be used to directly probe the number of species, the atom coordination, and connectivity. ^{31}P is an $I = 1/2$ nucleus with 100% natural abundance, and the strong magnetogyric ratio (10.84×10^7 rad s^{-1} T^{-1}) is thus readily observable. Strong correlations may be found among the NMR observables (mainly chemical shift) and the structural features, which are particularly useful for phosphate chemistry.[30,31]

^{31}P measurements were acquired for the Zn1 composition to clarify the crystal nature of the sample. The experimental spectrum is reported in Figure 2 together with the proposed best fit. ^{31}P NMR spectra are generally dominated by chemical shift anisotropy (CSA). The CSA contribution is well averaged by sample rotation giving origin to a pattern of spinning sidebands (see the inset in Figure 2), and the MAS spectrum highlights the isotropic resonances, which can be directly related to the distinct P sites present in the polymorph(s). The ^{31}P MAS spectra of the mixed Co/Zn compositions were much less informative because of the large paramagnetic interaction due to the transition metal unpaired electrons (see, for example, ref 32). Therefore, they will not be considered in the following study.

The ^{31}P NMR signals of $[PO_4]^{3-}$ moieties have been widely characterized and labeled with the nomenclature Q_n with n indicating the number of bridging oxygens, in analogy with the ^{29}Si case. The spectrum shows different lines in the chemical shift range −1, −3 ppm, compatible with a dimer $Q1$ [i.e., the P_2O_7 unit] phosphorus coordination.[30,31] The spectrum can be fitted by five distinct sites. Four of them are characterized by a similar area and line broadening, whereas the one at a higher

https://doi.org/10.1021/acs.jpcc.1c08753
J. Phys. Chem. C 2022, 126, 701−708

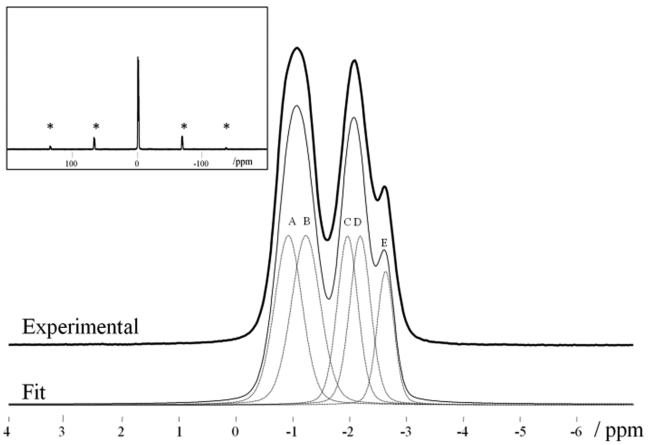

Figure 2. ^{31}P single pulse spectrum in the range from 4 to −6 ppm for the $Na_2ZnP_2O_7$ sample recorded at a spinning rate of 10 kHz, together with results from the best-fit procedure. In the inset, the same spectrum in the chemical shift range 200; −200 is reported, with evidence of spinning sidebands (*).

field is sharper and less intense, as reported in Table 1. As mentioned above, the small cell tetragonal system presents a

Table 1. ^{31}P NMR Parameters Obtained from the Analysis of the One-Pulse Spectrum; δ_{iso}: Isotropic Chemical Shift and FWHH: Full Width at Half Height

site	δ_{iso} (ppm)	FWHH (ppm)	area (%)	phase ratio
A	−1.16	0.58	23.4	∼2
B	−1.40	0.60	23.7	∼2
C	−2.27	0.43	20.6	∼2
D	−2.42	0.45	20.8	∼2
E	−2.89	0.34	11.5	∼1

single crystallographic site for phosphorus, whereas in the orthorhombic model four distinct P positions with the same multiplicity are found. The four peaks in the −1.16; −2.42 ppm range can thus be attributed to the four P atoms in the orthorhombic cell, whereas the smallest peak at −2.89 ppm can be associated to the unique tetragonal phosphorus position. Considering the ratio between the different contributions, the orthorhombic/tetragonal ratio in terms of the phase percentage is ∼2:1 as the four peaks observed in the −1.16; −2.42 ppm range are all related to the same crystal phase. The alternative possibility to have the coexistence of $Na_2ZnP_2O_7$ and $Zn_2P_2O_7$ phases,[33] because of partial Na loss during the heating treatments, can be ruled out. In fact, zinc pyrophosphate has monoclinic symmetry (space group I_2/c) and three nonequivalent P sites in the unit cell.[34] The ^{31}P NMR spectrum of this compound is characterized by three peaks in the region from −15.8 to −21.1 ppm,[35] where we did not observe any spectral feature. The differences in the chemical shift values between $Zn_2P_2O_7$ and the $Na_2ZnP_2O_7$ sample discussed in the present work arise from the different structures of the two compounds. Although the local environment of the P_2O_7 unit is the same in terms of the coordination number and connectivity, the differences in P−O bond lengths and PO_4 tetrahedron distortion can strongly affect the CSA term that in turn determines the position of the observed resonances.[36]

To validate the hypothesis of coexistence of the two polymorphs (tetragonal and orthorhombic), DFT calculations were performed to evaluate the relative phase stability of the two structures. The calculated structural parameters are in good agreement with literature data, where available, and with cell parameters obtained from analysis of the diffraction patterns, presented in the following sections (see Figure 3).

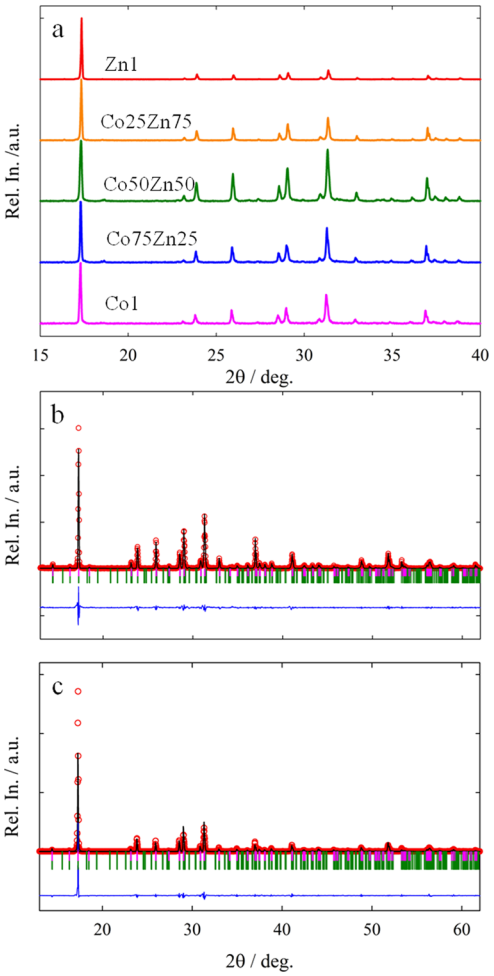

Figure 3. (a) X-ray powder diffraction patterns for the $Na_2(Co/Zn)P_2O_7$ series of samples. (b) Profile matching analysis for the Co25Zn75 composition with the experimental data (red circles), calculated profile (black line), difference between experimental and calculated data (blue line), and Bragg position for the tetragonal (pink bars) and orthorhombic (green bars) phases (χ^2 = 2.18). (c) Profile matching based on the small cell tetragonal and orthorhombic models for the Zn1 XRPD pattern.

The energy of the two polymorphs differs by only 0.08 eV (∼3 kT at the room temperature), with the orthorhombic one having the lowest energy. This result strongly supports the proposed analysis of the NMR data based on a mixture of polymorphs and suggests how, under the considered synthesis conditions, both phases are easily obtained for the Zn1 composition.

The orthorhombic model has not been proposed before for the Zn1 composition. However, it must be considered that the large cell tetragonal system presented by Belharouak et al.[17] is comparable with the orthorhombic one, as it uses a huge unit cell to account for the partially eclipsed stacking of the layers while maintaining the tetragonal symmetry. The orthorhombic model offers the same accurate description of this stacking, together with accounting for the modulation of the layers along

https://doi.org/10.1021/acs.jpcc.1c08753
J. Phys. Chem. C 2022, 126, 701−708

the *b*-axis. A comparison of the simulated XRPD patterns given by the three models and the experimental data is reported in Figure S1 of the Supporting Information (SI).

For the Co-containing composition, the NMR analysis did not provide sufficient information since the presence of Co^{2+} leads to a strong paramagnetic contribution dominating the global Hamiltonian. Figure S2 (Supporting Information) shows, as an example, the ^{31}P NMR data obtained for the Co50Zn50 composition. The interaction spans over 6000 ppm, hindering the possibility to obtain high-resolution data under the considered experimental conditions.

For the Co1 composition, in the absence of useful NMR data, a detailed investigation was performed by coupling XRPD and neutron diffraction analysis (see the next section). First, we considered the simulated neutron patterns generated from the tetragonal and orthorhombic cells compared with the experimental data (see Figure S3 in the Supporting Information). The presence of significant differences in both the number of reflections and the relative intensities allows us to identify the orthorhombic phase as the most suitable. Subsequent analysis of the neutron and XRPD data confirms this hypothesis, as satisfactory results can be obtained considering the orthorhombic cell (obtained profile matching agreement factors: $\chi^2_{ortho} = 3.02$, $\chi^2_{tetra} = 11.2$).

Based on the results for the two end members, the XRPD data (see Figure 3) of the whole series were analyzed. All the collected patterns look alike, as expected from the very similar crystal structures and from the small variation in the ionic radii of the metal ion in the two end members ($r(Co^{2+})IV = 0.58$ Å; $r(Zn^{2+})IV = 0.60$ Å[38]). The analysis of the diffraction patterns for the mixed compositions was performed considering three different possibilities: pure small cell tetragonal, pure orthorhombic, and a mixture of the two polymorphs. For each sample, the best model was selected based on the agreement factors. The Zn-rich compositions (x = 0.5, 0.75, and 1) consist of a mixture of two polymorphs. On the other hand, the Co75Zn25 and Co1 samples are monophasic, and the best results were obtained with the use of the orthorhombic model, as obtained from the neutron data for the Co1 composition.

Figure 4 reports the optimal structural parameters obtained for each composition. The unit cell parameters for the two end members are in the range of those previously reported for the Zn1 and Co1 composition in the tetragonal[17,18] and orthorhombic[13,29] space groups, respectively. The parameters here reported show a linear trend with the composition, indicating the formation of a solid solution for the whole range of x values for the orthorhombic polymorph. The cell volume decreases with the increasing amount of Zn. This trend might seem counterintuitive, as the Shannon ionic radius of Zn^{2+} in tetrahedral coordination (0.60 Å) is slightly larger than that of Co^{2+} (0.58 Å); however, a similar trend has been already reported for other solid solutions containing the Zn/Co couple in tetrahedral coordination with oxygen (e.g., $(Zn,Co)Al_2O_4$,[39] $(Zn,Co)_2SiO_4$,[40] and $Ca_2(Zn,Co)Si_2O_7$[41]) and attributed to a larger covalence degree of the Zn−O bond, due to the strong hybridization of sp^3 orbitals.[42] It is particularly interesting to note the close similarity between the orthorhombic and tetragonal structural parameters for the samples Co50Zn50, Co25Zn75, and Zn1, confirming that the two polymorphs are well related.

3.2. Co/Fe Series. Figure 5a presents the neutron diffraction patterns for the $Na_2(Co/Fe)P_2O_7$ series collected

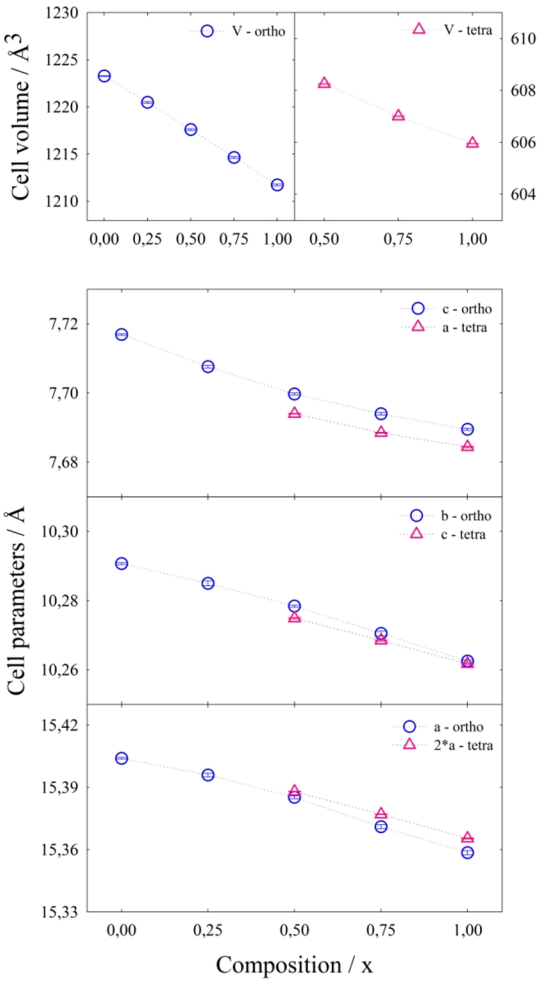

Figure 4. Cell parameters and cell volume as a function of the composition x with respect to the general formula $Na_2Co_{1-x}Zn_xP_2O_7$. Cell parameters are reported for the best structural model obtained for the analysis of each pattern: single phase orthorhombic for x = 0 and 0.25 and biphasic orthorhombic/tetragonal for x = 0.5, 0.75, and 1.

at room temperature. The patterns clearly show an evolution with the composition. The Co-rich samples give origin to relatively simple patterns, whereas the Fe-rich one show more complex diffraction data. Figure S4 (Supporting Information) reports the corresponding XRPD patterns of the same series whereas, Figure 5b shows the results of a profile matching analysis for the Co50Fe50 composition.

As already discussed in the previous section, the Co1 composition is treated as orthorhombic. For the Fe1 sample, in contrast, a 3D open framework structure defined by the $P1$[13,20] or P-1 symmetry was proposed.[5,10,21] Both the cases were checked against our data, and the P-1 symmetry emerged as the best structural model, as already reported for samples prepared under similar synthetic conditions.[3,5,15] The cell parameters obtained from the analysis for the whole series are reported in Figure 6.

The orthorhombic structure is maintained for the Co1, Co75Fe25, and Co50Fe50 samples. No extra peaks are found for the Co75Fe25 composition, and the sample can be considered pure and monophasic. Conversely, several extra peaks with low intensity are observed for the Co50Fe50 sample. These reflections can be attributed to the presence of

https://doi.org/10.1021/acs.jpcc.1c08753
J. Phys. Chem. C 2022, 126, 701−708

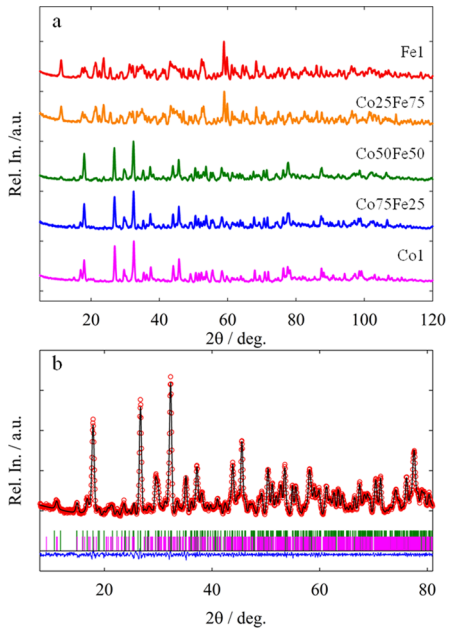

Figure 5. (a) Room temperature neutron diffraction patterns for the $Na_2(Co/Fe)P_2O_7$ series of samples. (b) Profile matching analysis for the Co50Fe50 composition with the experimental data (red circles), calculated profile (black line), difference between experimental and calculated data (blue line), and Bragg position for the triclinic (pink bars) and orthorhombic (green bars) phases (χ^2 = 1.45).

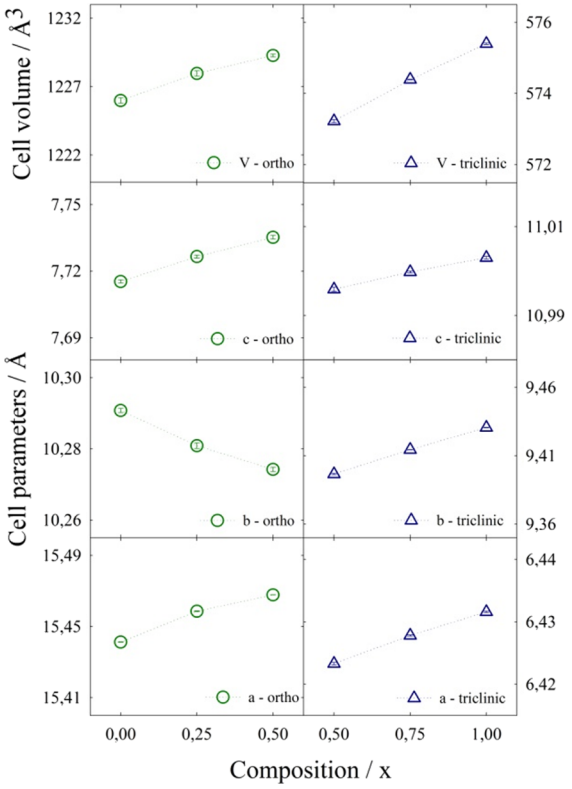

Figure 6. Cell parameters and cell volume as a function of the composition x with respect to the general formula $Na_2Co_{1-x}Fe_xP_2O_7$. Cell parameters are reported for both the polymorphs obtained as a function of the composition: orthorhombic (left panels) and triclinic (right panels).

the triclinic polymorph. Two-phase profile matching was performed to support this hypothesis and to exclude the possibility of impurities. The good quality of the profile matching analysis (see Figure 5b) confirms the coexistence of the two phases. The solubility limit of the Fe in the orthorhombic phase is slightly lower than 0.5 but higher than 0.25, as the cell parameters show a linear trend in the range $0.0 < x < 0.5$ (see Figure 6).

The cell parameters observed for the two end members are in good agreement with those previously reported for the same phases and the same compositions.[3,10,29] It must be considered that also for the pure compositions, a significant variability is found in the reported cell parameters (for example, the volume of the Fe1 sample is reported in the range 570.88[10]−581.05 Å[37]). These variations can be related to the thermal history of the sample and to the exact Na content in the structure.

The observed trend in both cell parameters and volume (see Figure 6) follows the variation of the average ionic radius of the M site with mixed Co/Fe occupancy ($r(Co^{2+})IV$ = 0.58 Å, $r(Fe^{2+})IV$ = 0.63 Å, and $r(Fe^{2+})VI$ = 0.61 Å[38]); thus, the increase of Fe content gives origin to a slight overall expansion of the cell for both the observed polymorphs. In addition, the transition from the orthorhombic to the triclinic polymorph as the Fe content increases may be related to the different electronic structures of Fe^{2+} (d^6) and Co^{2+} (d^7) and their consequent preferred coordination with oxygen, based on the crystal field theory. In particular, a d^6 ion will be highly stabilized in the octahedral environment found in the $Na_2FeP_2O_7$ triclinic structure compared to the tetrahedral coordination found in the tetragonal and orthorhombic polymorphs. Table 2 reports in a schematic way a summary of the polymorphs present in the two series.

Table 2. Summary of the Polymorphs Presents as a Function of Composition for the $Na_2(Co/Zn)P_2O_7$ and $Na_2(Co/Fe)P_2O_7$ Series

compound	tetragonal ($P4_2/mnm$)	orthorhombic ($P2_1cn$)	triclinic ($P\text{-}1$)
$Na_2ZnP_2O_7$	×	×	
$Na_2Zn_{0.75}Co_{0.25}P_2O_7$	×	×	
$Na_2Zn_{0.50}Co_{0.50}P_2O_7$	×	×	
$Na_2Zn_{0.25}Co_{0.75}P_2O_7$		×	
$Na_2CoP_2O_7$		×	
$Na_2Co_{0.75}Fe_{0.25}P_2O_7$		×	
$Na_2Co_{0.50}Fe_{0.50}P_2O_7$		×	×
$Na_2Co_{0.25}Fe_{0.75}P_2O_7$			×
$Na_2FeP_2O_7$			×

4. CONCLUSIONS

The series $Na_2(M/M')P_2O_7$ with couples M/M' = Co/Zn and Co/Fe were prepared according to a standard solid-state chemistry route, already reported in the literature for the pure end members. Different models were reported for the description of these compositions, and contradictory information emerged from previous studies. The combination of several structural investigation techniques (solid-state NMR, diffraction, and DFT calculations) led us to a better understanding of the crystal chemistry of the considered series. These analyses led us to highlight similarities between related structures (tetragonal and orthorhombic) and to explore the evolution of the systems with the M species. For

https://doi.org/10.1021/acs.jpcc.1c08753
J. Phys. Chem. C 2022, 126, 701−708

both the series, a phase transition as a function of the composition is observed. While for the Zn-rich samples, the tetragonal and orthorhombic structures are observed, the samples with high Co content are defined as orthorhombic, whereas moving to the Fe end member the triclinic *P*-1 structure is obtained.

Despite the fact that the ionic radii do not dramatically change moving from Zn to Fe, the variation of the metal species on the M site leads to a rearrangement of the structure. In the tetragonal system, the M ion is found in an undistorted tetrahedral coordination that becomes distorted−tetrahedral in the orthorhombic structure, whereas in the triclinic space group the M site is in octahedral coordination. The phase transitions observed moving from Zn, Co to Fe can be due to the mutual effect of the cation size and the crystal field stabilization of *d* orbitals of the M^{2+} transition metal ion.

Finally, the DFT calculations revealed that the tetragonal and orthorhombic phases are characterized by similar formation energy for the Zn1 composition. Thus, the final structures may be strongly dependent upon the synthesis procedure, heating treatments, and cooling rates. Further work is needed to identify how to selectively crystallize the desired phase.

■ ASSOCIATED CONTENT

Supporting Information

The Supporting Information is available free of charge at https://pubs.acs.org/doi/10.1021/acs.jpcc.1c08753.

> Experimental and calculated XRPD patterns for $Na_2ZnP_2O_7$ according to the small cell tetragonal and large cell tetragonal models; experimental and calculated XRPD diffraction patterns for $Na_2CoP_2O_7$ according to the tetragonal and orthorhombic models; ^{31}P single pulse NMR spectrum for $Na_2Zn_{0.5}Co_{0.5}P_2O_7$; and room temperature XRPD patterns for the $Na_2(Co/Fe)P_2O_7$ series (PDF)

■ AUTHOR INFORMATION

Corresponding Author

Cristina Tealdi − *Department of Chemistry, University of Pavia and INSTM-UdR Pavia, Pavia 27100, Italy;* orcid.org/0000-0003-1700-1723; Email: cristina.tealdi@unipv.it

Authors

Chiara Ferrara − *Department of Materials Science, University of Milano-Bicocca, Milano 20125, Italy*

Clemens Ritter − *Institut Laue-Langevin, Grenoble F-38042, France*

Piercarlo Mustarelli − *Department of Materials Science, University of Milano-Bicocca, Milano 20125, Italy;* orcid.org/0000-0001-9954-5200

Complete contact information is available at: https://pubs.acs.org/10.1021/acs.jpcc.1c08753

Author Contributions

The manuscript was written through contributions of all authors. All authors have given approval to the final version of the manuscript.

Notes

The authors declare no competing financial interest.

■ ACKNOWLEDGMENTS

Financial support from the Italian Government, Ministry of Education, Universities and Research MIUR (PRIN N° 2017MCEEY4 funding) and by Fondazione Cariplo-Regione Lombardia through grant 2015-0753 is gratefully acknowledged.

■ REFERENCES

(1) Nishimura, S.; Nakamura, M.; Natsui, R.; Yamada, A. New Lithium Iron pyrophosphate as 3.5 V class cathode material for Lithium ion battery. *J. Am. Chem. Soc.* **2010**, *132*, 13596−13597.

(2) Erragh, F.; Boukhari, A.; Abraham, F.; Elouadi, B. The crystal structure of α- and β-$Na_2CuP_2O_7$. *J. Solid State Chem.* **1995**, *120*, 23−31.

(3) Kim, H.; Shakoor, R. A.; Park, C.; Lim, S. Y.; Kim, J. S.; Jo, Y. N.; Cho, W.; Miyasaka, K.; Kahraman, R.; Jung, Y.; Choi, J. W. $Na_2FeP_2O_7$ as a promising Iron-based pyrophosphate cathode for sodium rechargeable batteries: A combined experimental and theoretical study. *Adv. Funct. Mater.* **2013**, *23*, 1147−1155.

(4) Barpanda, P.; Lu, J.; Ye, T.; Kajiyama, M.; Chung, S. C.; Yabuuchi, N.; Komaba, S.; Yamada, A. A layer-structured $Na_2CoP_2O_7$ pyrophosphate cathode for sodium-ion batteries. *RSC Adv.* **2013**, *3*, 3857−3860.

(5) Tealdi, C.; Ricci, M.; Ferrara, C.; Bruni, G.; Berbenni, V.; Quartarone, E.; Mustarelli, P. Glucose-assisted synthesis and wet-chemistry preparation of pyrophosphate cathodes for rechargeable Na-ion batteries. *RSC Adv.* **2016**, *6*, 99735−99742.

(6) Gond, R.; Vanam, S. P.; Barpanda, P. $Na_2MnP_2O_7$ polymorphs as efficient bifunctional catalysts for oxygen reduction and oxygen evolution reactions. *Chem. Commun.* **2019**, *55*, 11595−11598.

(7) Song, H. J.; Yoon, H.; Ju, B.; Kim, D.-W. Sodium-nickel pyrophosphate as a novel oxygen evolution electrocatalyst in alkaline medium. *J. Am. Ceram. Soc.* **2020**, *103*, 4748−4753.

(8) Belbal, R.; Gacem, L.; Bentria, B.; Ait Ahsaine, H.; Soltani, M. T.; Saidat, B.; Ghezal, E. A.; Gueddim, A.; Guerbous, L. Synthesis and luminescence spectroscopy study of a novel orange-red colour emissions phosphor based on Tb^{3+} ion-doped $Na_2ZnP_2O_7$. *Luminescence* **2021**, *36*, 489−496.

(9) Sanz, F.; Parada, C.; Rojo, J. M.; Ruiz-Valero, C.; Saez-Puche, R. Studies on tetragonal $Na_2CoP_2O_7$, a novel ionic conductor. *J. Solid State Chem.* **1999**, *145*, 604−611.

(10) Jung, Y. H.; Lim, C. H.; Kim, J. H.; Kim, D. K. $Na_2FeP_2O_7$ as a positive electrode material for rechargeable aqueous sodium-ion batteries. *RSC Adv.* **2014**, *4*, 9799−9802.

(11) Clark, J. M.; Barpanda, P.; Yamada, A.; Islam, M. S. Sodium-ion battery cathodes $Na_2FeP_2O_7$ and $Na_2MnP_2O_7$: diffusion behaviour for high rate performance. *J. Mater. Chem. A* **2014**, *2*, 11807−11812.

(12) Niu, Y.; Zhang, Y.; Xu, M. A review on pyrophosphate framework cathode materials for sodium-ion batteries. *J. Mater. Chem. A* **2019**, *7*, 15006−15025.

(13) Erragh, F.; Boukhari, A.; Elouadi, B.; Holt, E. M. Crystal structures of two allotropic forms of $Na_2CoP_2O_7$. *J. Cryst. Spect. Res.* **1991**, *21*, 321−326.

(14) Beaury, L.; Derouet, J.; Binet, L.; Sanz, F.; Ruiz-Valero, C. The blue allotropic form of Co^{2+}:$Na_2CoP_2O_7$: optical and magnetic properties, correlation with crystallographic data. *J. Solid State Chem.* **2004**, *177*, 1437−1443.

(15) Tealdi, C.; Ricci, M.; Ferrara, C.; Bruni, G.; Quartarone, E.; Mustarelli, P. Electrochemical study of $Na_2Fe_{1-x}Mn_xP_2O_7$ (x = 0, 0.25, 0.5, 0.75, 1) as cathode material for rechargeable Na-ion batteries. *Batteries* **2016**, *2*, 1.

(16) Barpanda, P.; Liu, G.; Mohamed, Z.; Ling, C. D.; Yamada, A. Structural, magnetic and electrochemical investigation of novel binary $Na_{2-x}(Fe_{1-y}Mn_y)P_2O_7$ ($0 \le y \le 1$) pyrophosphate compounds for rechargeable sodium-ion batteries. *Solid State Ionics* **2014**, *268*, 305−311.

(17) Belharouak, I.; Gravereau, P.; Parent, C.; Chaminade, J. P.; Lebraud, E.; Le Flem, G. Crystal Structure of $Na_2ZnP_2O_7$: reinvestigation. *J. Solid State Chem.* **2000**, *152*, 466−473.
(18) Erragh, F.; Boukhari, A.; Abderahim, S.; Holt, E. M. Disodium Zinc pyrophosphate and Disodium (Europium) Zinc pyrophosphate. *Acta Cryst.* **1998**, *C54*, 1373−1376.
(19) Kumar, B. V.; Vithal, M. Luminescence (M = Mn^{2+}, Cu^{2+}) and ESR (M = Gd^{3+}, Mn^{2+}, Cu^{2+}) of $Na_2ZnP_2O_7$: M. *Phys. B Condens. Matter* **2012**, *407*, 2094−2099.
(20) Lokanath, N. K.; Sridhar, M. A.; Prasad, J. S.; Gopalakrishna, G. S.; Ashamanjari, K. G. Synthesis and structural characterization of $(Na_2CoP_2O_7)_2$ crystal. *J. Mater. Sci. Lett.* **1999**, *18*, 1723−1726.
(21) Chen, C.-Y.; Matsumoto, K.; Nohira, T.; Hagiwara, R.; Orikasa, Y.; Uchimoto, Y. Pyrophosphate $Na_2FeP_2O_7$ as a low-cost and high-performance positive electrode material for sodium secondary batteries utilizing an inorganic ionic liquid. *J. Power Sources* **2014**, *246*, 783−787.
(22) le Bail, A.; Duroy, H.; Fourquet, J. L. Ab-initio structure determination of $LiSbWO_6$ by X-ray powder diffraction. *Mater. Res. Bull.* **1988**, *23*, 447−452.
(23) Rietveld, H. M. A profile refinement method for nuclear and magnetic structures. *J. Appl. Crystallogr.* **1969**, *2*, 65−71.
(24) Rodriguez-Carvajal, J. Recent advances in magnetic structure determination by neutron powder diffraction. *Phys. B Condens. Matter.* **1993**, *192*, 55−69.
(25) Massiot, D.; Fayon, F.; Capron, M.; King, I.; le Calvé, S.; Alonso, B.; Durand, J. O.; Bujoli, B.; Gan, Z.; Hoatson, G. Modelling one- and two-dimensional solid-state NMR Spectra. *Magn. Reson. Chem.* **2002**, *40*, 70−76.
(26) Giannozzi, P.; Baroni, S.; Bonini, N.; Calandra, M.; Car, R.; Cavazzoni, C.; Ceresoli, D.; Chiarotti, G. L.; Cococcioni, M.; Dabo, I.; Dal Corso, A.; de Gironcoli, S.; Fabris, S.; Fratesi, G.; Gebauer, R.; Gerstmann, U.; Gougoussis, C.; Kokalj, A.; Lazzeri, M.; Martin-Samos, L.; Marzari, N.; Mauri, F.; Mazzarello, R.; Paolini, S.; Pasquarello, A.; Paulatto, L.; Sbraccia, C.; Scandolo, S.; Sclauzero, G.; Seitsonen, A. P.; Smogunov, A.; Umari, P.; Wentzcovitch, R. M. QUANTUM ESPRESSO: a modular and open-source software project for quantum simulations of materials. *J. Phys.: Condens. Matter* **2009**, *21*, No. 395502.
(27) Perdew, J. P.; Burke, K.; Ernzerhof, M. Generalized gradient approximation made simple. *Phys. Rev. Lett.* **1996**, *77*, 3865.
(28) Ben Rhaiem, A.; Hlel, F.; Guidara, K.; Gargouri, M. Electrical conductivity and dielectric analysis of $AgNaZnP_2O_7$ compound. *J. Alloys Compd.* **2009**, *485*, 718−723.
(29) Barpanda, P.; Avdeev, M.; Ling, C. D.; Lu, J.; Yamada, A. Magnetic structure and properties of the $Na_2CoP_2O_7$ pyrophosphate cathode for Sodium-ion batteries: A supersuperexchange-driven non-collinear antiferromagnet. *Inorg. Chem.* **2013**, *52*, 395−401.
(30) Turner, G. L.; Smith, K. A.; Kirkpatrick, R. J.; Oldfield, E. Boron-11 nuclear magnetic resonance spectroscopic study of borate and borosilicate minerals and a borosilicate glass. *J. Magn. Reson. Ser. B* **1986**, *67*, 544−550.
(31) Mustarelli, P. The NMR information on phosphate glasses: a review. *Phosphorus Res. Bull.* **1999**, *10*, 25−36.
(32) Mustarelli, P.; Massarotti, V.; Bini, M.; Capsoni, D. Transferred hyperfine interaction and structure in $LiMn_2O_4$ and Li_2MnO_3 coexisting phases: A XRD and ^7Li NMR-MAS study. *Phys. Rev. B* **1997**, *55*, 12018−12024.
(33) Petrova, M. A.; Mikirticheva, G. A.; Grebenshchikov, R. G. Phase equilibria in the $Zn_2P_2O_7$ − $M_2ZnP_2O_7$ and $M_2'ZnP_2O_7$ − $M_2''ZnP_2O_7$ (M, M', M" = Li, Na, K) glass-forming systems. *Inorg. Mater.* **2007**, *43*, 1024−1031.
(34) Robertson, B. E.; Calvo, C. Crystal structure of α-$Zn_2P_2O_7$. *J. Solid State Chem.* **1970**, *1*, 120−133.
(35) Jarboui, A.; Ben Rhaeim, A.; Hlel, F.; Guidara, K.; Gargouri, M. NMR study and electrical properties investigation of $Zn_2P_2O_7$. *Ionics* **2010**, *16*, 67−73.
(36) Un, S.; Klein, M. P. Study of ^{31}P NMR chemical shift tensor and their correlation to molecular structure. *J. Am. Chem. Soc.* **1989**, *111*, 5119−5124.
(37) Barpanda, P.; Liu, G.; Ling, C. D.; Tamaru, M.; Avdeev, M.; Chung, S. C.; Yamada, Y.; Yamada, A. $Na_2FeP_2O_7$: A safe cathode for rechargeable sodium-ion batteries. *Chem. Mater.* **2013**, *25*, 3480−3487.
(38) Shannon, R. D. Revised effective ionic radii and systematic studies of interatomic distances in halides and chalcogenides. *Acta Crystallogr. A* **1976**, *32*, 751−767.
(39) Ardit, M.; Cruciani, G.; Dondi, M. Structural relaxation in tetrahedrally coordinated Co^{2+} along the gahnite-Co-Aluminate spinel solid solution. *Am. Mineral.* **2021**, *97*, 1397−1401.
(40) Ozel, E.; Yurdakul, H.; Turan, S.; Ardit, M.; Cruciani, G.; Dondi, M. Co-doped willemite ceramic pigments: Technological behaviour, crystal structure and optical properties. *J. Eur. Ceram. Soc.* **2010**, *30*, 3319−3329.
(41) Dondi, M.; Zanelli, C.; Ardit, M.; Cruciani, G. Co-Doped Hardystonite, $Ca_2(Zn,Co)Si_2O_7$, a new blue ceramic pigment. *J. Am. Ceram. Soc.* **2011**, *94*, 1025−1030.
(42) Louisnathan, S. J. Refinement of the crystal structure of hardystonite, $Ca_2ZnSi_2O_7$. *Z. Kristallogr. Cryst. Mater.* **1969**, *130*, 427−437.

https://doi.org/10.1021/acs.jpcc.1c08753
J. Phys. Chem. C 2022, 126, 701−708